Thermal Deformation Measurement of Aerospace Honeycomb Panel Based on Fusion of 3D-Digital Image Correlation and Finite Element Method

Linghui Yang [1,2,*] , Zezhi Fan [1,2], Ke Wang [3], Hui Sun [3], Shuotao Hu [4] and Jigui Zhu [1,2]

1   State Key Laboratory of Precision Measuring Technology and Instruments, School of Precision Instrument and Opto-Electronics Engineering, Tianjin University, Tianjin 300072, China
2   School of Precision Instrument and Opto-Electronics Engineering, Tianjin University, Tianjin 300072, China
3   Shanghai Institute of Spacecraft Equipment, Shanghai Academy of Spaceflight Technology, Shanghai 200240, China
4   Beijing Institute of Radio Measurement, Beijing 100854, China
*   Correspondence: icelinker@tju.edu.cn

Abstract: Aiming to solve the problem of the high-precision deformation measurement of large-scale satellite structures in manufacturing and testing environments, this paper proposes a measurement method based on the idea of fusing actual measurements with finite element analysis. The digital image correlation (DIC) method is used to obtain the high-precision deformation of the honeycomb panel, and the finite element method (FEM) model is introduced to remove the limitations of existing pure measurement methods. Data fusion based on a machine learning neural network is proposed to fuse high-precision deformation and physical information such as temperature to conduct multi-level training on FEM parameters. Through an interpolation of the analysis and calculation results after training, not only can the accuracy of the finite element be improved, but difference and extrapolation of the digital image correlation measurement results can be performed. In the experiments, the satellite on-orbit temperature data are substituted into the modified finite element model. The testing results shows that the prediction accuracy of the model under different temperature loads can be controlled within 10 μm under an 840 mm × 640 mm scale. A high predictive accuracy can be achieved for the revised model for the complete deformation of large structural sections.

Keywords: thermal deformation; digital image correlation; finite element method; neural network; data fusion

1. Introduction

With continuous increases in the demands regarding satellites' observation accuracy and working stability, the problem of the micron-scale deformation of large-scale honeycomb panels is receiving widespread attention [1–3]. Since satellites are always exposed in a harsh in-orbit environment with high- and low-temperature changes, strong radiation and weightlessness, structural deformations are inevitable. When the key installation or reflective surface of a satellite structure is thermally deformed, the change in the relative position and angle of payload equipment may seriously degrade the performance or even lead to failure in the entire satellite. Therefore, monitoring the deformation of the satellite's structure is of great significance to ensure the high performance and stable operation of a satellite [4–11].

Since the working environment of a satellite is complex, researchers have tried to study the thermal deformation of satellite structure through a variety of methods, which can generally be divided into two aspects: actual testing and simulation analysis. Actual testing is usually conducted by instruments and sensors in a test environment, mainly including a piezoelectric strain sensor [12], fibre Bragg grating [13,14], electronic speckle

pattern interferometry [15], active infrared thermal imaging technology [16], shearography [17], scanning laser Doppler vibrometry (SLDV) [18] and the digital image correlation (DIC) method [19,20]. Piezoelectric strain sensors and fibre Bragg grating sensors need to be mounted on the surface of the structure; these can be highly integrated with the satellite but can only measure discrete deformation data. Piezoelectric strain sensors are often considered to have low precision, require many wirings, and have a limited range, and are susceptible to electromagnetic interference. Fibre Bragg grating sensors are more flexible during installation but the Bragg grating will be completely erased when the fibre temperature reaches a certain threshold; therefore, the thermal insulation must be seriously considered, which greatly increases the difficulty of the overall satellite design. Compared to the above method, active infrared thermal imaging, shearography, SLDV, electronic speckle pattern interferometry and digital image correlation are all based on the optoelectronic measurement principle, which is non-contact, with the advantages of high speed and high precision. This is a research hotspot at present. Active infrared thermal imaging technology is a fast and accurate non-destructive testing technology. These technologies are relatively low-cost and, combined with advanced signal processing tools, can successfully evaluate various types of material defects. However, active infrared thermography is still insensitive to deep damage and microcracks ranging from 10 µm to several millimeters in size [21]. Shearography and electronic speckle pattern interferometry can detect the displacement and deformation of the object surface using the speckle formed in space when coherent light shines on the rough object's surface. De Angelis et al. [22] used shearing photography to evaluate the defect depth of composite materials used in aviation. Shear speckle is very suitable for detecting object defects but will lead to a loss of correlation between speckle due to excessive rigid body motion. SLDV is used to study the interaction between guided waves and cracks, as well as holes and slits in metal plates, and can be used to measure strain and stress. Pawel Kudella et al. [18] applied SLDV to the delamination detection of composite structures, and provided the measurement results of simple composite plates, honeycomb core plates and actual stiffened composite plates through experiments. The DIC method, based on the principle of visual measurement, can achieve a micron-level accuracy and perform dynamic measurement. However, when determined by principle, the measurement range and resolution of the existing DIC measuring systems are usually limited by the image sensor, struggle to measure discontinuous complex structures and may be affected by environment interference. Thus, these methods are mostly used for single-material, small-component measurements in the laboratory environment. Unlike actual ground testing, the finite element simulation method is based on a digital model and finite element analysis, and has the advantages of not being affected by field conditions, full-field data acquisition, and adjustable multi-resolution. This is the main deformation analysis method in the current design stage [23–26]. Stephen M Merkowitz et al. carried out optical–mechanical thermal modelling and analysis for the Lisa satellite [27]. The temperature field of thermal deformation analysis was simulated by I-IDEA software. Róbert Kovács et al. conducted a thermal analysis of the SMOG-1 satellite using the finite element model method [28]. The mapping method of the temperature field, from thermal analysis software to structural analysis software, is mentioned in the load design manual of ESA [29]. The bottleneck of the FEM method comes from the fact that it can only use digital design models in most cases; the empirical parameters used in FEM simulation differ from the physical entity, resulting in limited simulation accuracy.

Different from the material mechanics measurement of a small, single part in the laboratory environment, the aerospace honeycomb panel is a kind of large-scale structural part with a discontinuous internal material structure and external dimensions that are usually more than 1 m. The use of a single DIC or FEM method has obvious limitations in device deformation analysis and measurement problems. However, if the advantages of the two methods are combined, it will undoubtedly be very attractive to solve the above problems. Therefore, research on the combination of DIC and FEM has been the focus of common attention in the fields of manufacturing, mechanics, materials and measurement in recent

years [30–33], and similar concepts have attracted the attention of many scholars [34,35]. The most common method is to use the measurement results to correct the finite element parameters, making them close to the real material characteristics. Although the accuracy of this method can be improved, it is still essentially a series of two single measurement methods. There is a sequential relationship in the process, and the correction results are limited by the accuracy of the finite element model and the DIC measurement accuracy; therefore, the data are not efficiently integrated.

In this paper, taking aerospace honeycomb panels as the testing object, a data fusion method based on machine learning is proposed, which introduces a neural network, selects several local high-precision deformations measured by DIC, and fuses physical information such as temperature to construct a training set and conduct multi-level training on FEM parameters. Through an interpolation of the analysis and calculation results after training, the accuracy of the finite element can be improved, and the difference and extrapolation of the DIC measurement results can be determined, so that the measurement system has the accuracy advantages of DIC and the coverage capability of FEM. Therefore, it can effectively solve the above deformation measurement problems. The remaining parts of this paper are organized as follows. In Section 2, the finite element correction method is described in detail, including the digital image correlation (DIC) method, the design of the BP neural network, and the design of the finite element optimization model. Section 3 presents the experiments verifying the accuracy of the 3D-DIC system and finite element model modification. Finally, the conclusions of this study are reported in Section 4.

2. Methods

According to the measurement requirements in the space environment, a measurement that hybridizes physical measurement and finite element model computing is proposed. This section provides an account of a spatial structure measurement method based on the digital image correlation measurement method and finite element model correction method. A flow chart of this method is shown in Figure 1. The upper left corner of Figure 1 shows the 3D-DIC system. The measured deformation field in the figure is the displacement field that is measured by the measuring system (the X direction). The right side of Figure 1 shows the finite element model established using material properties. The lower part of Figure 1 is the accurate finite element model obtained after fusion calculation. Using the neural network as a parameter mapping method, a high-precision deformation fitting method based on a mechanical finite element model was studied. The global deformation field of the spacecraft structure in space environment was reconstructed by combining the digital correlation three-dimensional deformation measurement data. Finally, the modified finite element model accurately predicted the structural deformation prediction of the satellite under different temperature environments. Thus, it has the function of monitoring the stability of key satellite structures in a space environment.

2.1. 3D Digital Image Correlation

The imaging model of a single camera is the basis of binocular camera stereo vision. A typical camera imaging model is shown in Figure 2. Four coordinate systems are defined in the model:

1. World coordinate system O_w with a point in real space as the origin.
2. Camera coordinate system O_c with the camera optical center position as the origin.
3. Imaging plane coordinate system O_s taking the intersection point of optical axis and imaging plane as the origin.
4. Image coordinate system O_i with the upper left corner of the imaging pixel array plane as the origin.
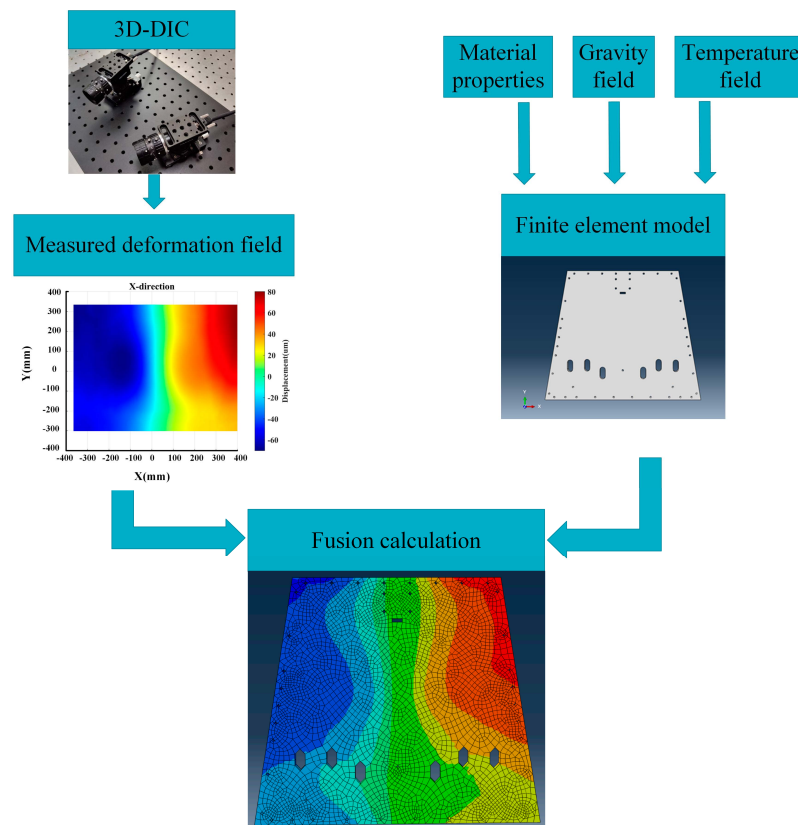
Figure 1. Flow chart of finite element model correction method.
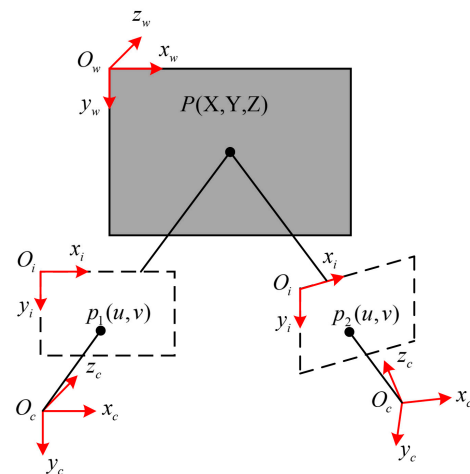
Figure 2. Coordinate system conversion.

Let coordinate M of the space point in the world coordinate system be (X_w, Y_w, Z_w), the coordinate system's mapping transformation to the image coordinate system is point m; the coordinate is (u, v). The mapping transformation relationship of two points is shown in the following formula

$$\alpha \begin{bmatrix} u \\ v \\ 1 \end{bmatrix} = \begin{bmatrix} f_x & 0 & u_0 & 0 \\ 0 & f_y & v_0 & 0 \\ 0 & 0 & 1 & 0 \end{bmatrix} \begin{bmatrix} R_{11} & R_{12} & R_{13} & t_x \\ R_{21} & R_{22} & R_{23} & t_y \\ R_{31} & R_{32} & R_{33} & t_z \\ 0 & 0 & 0 & 1 \end{bmatrix} \begin{bmatrix} X_w \\ Y_w \\ Z_w \\ 1 \end{bmatrix} \tag{1}$$

where $f_x = f/d_x$, $f_y = f/d_y$ and two parameters are the normalized focal length of the camera; dx and dy, respectively, represent the distance of adjacent pixels in the image coordinate system in the x and y directions; (u_0, v_0) is the coordinate where the optical axis intersects the imaging plane; R is the coordinate system rotation matrix; and T is the coordinate system translation vector.

The binocular vision system is based on the imaging theory of a single camera, and combines the information of two cameras with different viewing angles. The transformation relationship between the image coordinate system of two single cameras and the world coordinate system is solved, and then, according to the calibrated camera's internal and external parameters, the pixel coordinates of two cameras can be fused and matched to calculate and reconstruct the three-dimensional coordinates of the space points in the world coordinate system.

The two-dimensional digital image correlation method obtains the displacement of the corresponding centerpoint by matching the sub-regions in the speckle image of the object surface before and after deformation. The specific steps are to establish the shape function and correlation function of the image's sub-region, and then iteratively calculate the extreme value of the correlation function. In this paper, the first-order shape function is used to describe the deformation sub-region, as shown in the following equation.

$$w_1(\overrightarrow{x}, \Delta\overrightarrow{p}) = \begin{bmatrix} 1+\Delta u_x & \Delta u_y & \Delta u \\ \Delta v_x & 1+\Delta v_y & \Delta v \\ 0 & 0 & 1 \end{bmatrix} \begin{bmatrix} \Delta x \\ \Delta y \\ 1 \end{bmatrix} \tag{2}$$

$$\overrightarrow{p} = (u, u_x, u_y, v, v_x, v_y) \tag{3}$$

In the formula: u, v are the displacement of the centerpoint of the image sub-area in the x, y direction, u_x, u_y, v_x, u_y represent the strain of the image sub-area. Mainstream sub-pixel displacement measurement algorithms include the gradient method, Newton–Raphson method [36], Inverse compositional matching strategy and Gauss–Newton (ICGN) method [37]. Among them, the ICGN method is the most widely used. The ICGN method use an inverse synthesis matching method to update the affine deformation function. The form of the zero-mean normalized sum squared difference (ZNSSD) based on the first-order shape function is:

$$C_{ZNSSD}(\Delta p_1) =$$
$$\sum_{x=-M}^{M} \sum_{y=-M}^{M} \left\{ f(W_1(W_{1s}(x,y;\Delta p_1);0)) - \overline{f} - \frac{\Delta(fg)}{\Delta(g^2)} \left[g(W_1(x,y;p_1^n)) - \overline{g} \right] \right\}^2 \tag{4}$$

In the formula: $W_1(W_{1s}(x,y;\Delta p_1);0)$ is the shape function of the reference sub-area, $g(W_1(x,y;p_1^n))$ is the shape function of the next iteration of the deformation sub-area, $\overline{f}$ is the average gray value of the reference sub-area, and $\overline{g}$ is the average gray value of the deformed sub-area. The iterative process of the IC-GN method is shown in Figure 3. During each iteration, the incremental deformation $W_1(x,y;\Delta p_1)$ is superimposed on the reference subset, and the target subset is updated after transformation. In the ICGN method, the Hessian matrix is only related to the original region and only needs to be calculated once. Therefore, the ICGN method hugely improves computational efficiency.

The 3D digital image correlation method combines binocular vision with the 2D digital image correlation method. The 3D reconstruction uses the internal and external parameters of the dual camera calculated during the camera calibration process and the point pairs calculated by matching the 2D speckle image to reconstruct the 3D point cloud and obtain 3D coordinate points and 3D displacement. The principle is shown in Figure 4. When the object is not deformed, the left and right cameras capture two images of the object. The sub-region of the left camera, centered on (X_{L0}, Y_{L0}), is selected, and the two images are stereo-matched according to the binocular vision model. Then, the three-dimensional coordinate (X_1, Y_1, Z_1) of the sub-region is reconstructed according to

the internal and external parameters of the calibrated dual cameras. The left and right cameras take two images of the deformed object. The corresponding deformation sub-region (X_{L1}, Y_{L1}) is obtained by computing the image correlation of the corresponding pre-deformation and post-deformation images. After finding the matching sub-region, the algorithm reconstructs the 3D coordinate (X_2, Y_2, Z_2) of the deformed sub-region. Finally, the three-dimensional displacement data are obtained by subtracting the coordinates before and after the deformation of the corresponding sub-region.
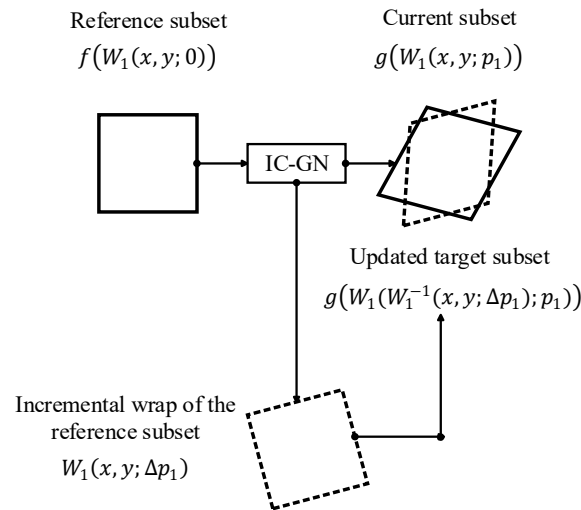
Figure 3. Iteration process of IC-GN method.
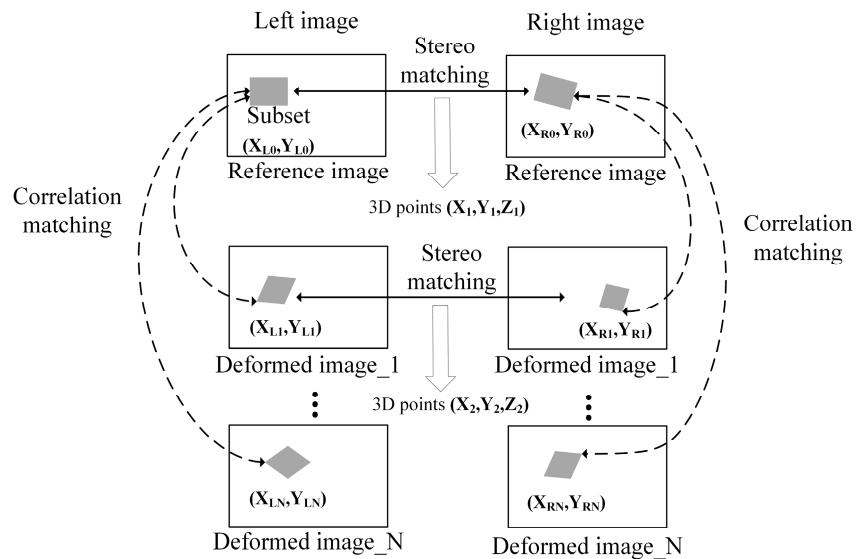
Figure 4. 3D-DIC measurement principle.

2.2. Finite Element Model Modification Method

The results obtained from the simplified finite element model often have errors when compared to the actual situation. Therefore, the initial finite element model needs to be modified. In essence, the finite element model correction problem is a multivariate function constraint optimization problem. The difference between the characterized measurement results and the calculated results is the goal of optimization. Appropriate constraints are introduced to optimize the structural and state parameters. Finally, the theoretical calculation value of the structure approximates the measured value of the load experiment. Using an implicit mathematical expression with forward differencing, the sensitivity analysis method analyzes the degree of influence of the selected parameters on the final results. For

the satellite structure, four main types of parameters are required to build the initial finite element model, as follows:

1. Geometry parameters: the size and the thickness of the skin.
2. Material property parameters: expansion coefficient, Poisson's ratio.
3. Boundary condition parameters: constraint point location.
4. Load parameters: temperature load on the structure.

Establishing an appropriate objective function is an important link in the process of finite element model correction. The goal of model correction is to make the calculated model results approach the actual measured values. Therefore, the amount that characterizes the difference between the calculated values of the model and the measured values is generally taken as the objective function. The error value between the model simulation value sim_{ui} and the actual measurement value u_i is defined as err_i. The optimization model is constructed as follows.

$$\left\{ sim_{ui} : \left(sim_{dx_i}, sim_{dy_i}, sim_{dz_i} \right), i = 1 \sim n \right\} \tag{5}$$

$$\left\{ u_i : (dx_i, dy_i, dz_i), i = 1 \sim n \right\} \tag{6}$$

$$\left\{ err_i : \left(sim_{dx_i} - dx_i, sim_{dy_i} - dy_i, sim_{dz_i} - dz_i \right), i = 1 \sim n \right\} \tag{7}$$

$$\begin{cases} \min F(X) = \sum\limits_{i=1}^{n} err_i{}^2 \\ \qquad s.t. \\ \underline{A} \leq A \leq \overline{A} \\ \underline{S} \leq S \leq \overline{S} \end{cases} \tag{8}$$

A is the design variable, including the geometric parameters and material properties of the tested structure. $\underline{A}$ and $\overline{A}$ are the upper and lower limits of design variable A. S is the state variable, including boundary condition parameters. $\underline{S}$ and $\overline{S}$ are the upper and lower limits of state variable S. Parameter n is the number of selected feature points.

2.3. Design of Fusion Algorithm

As a typical complex sandwich structure, the FEM correction of the honeycomb panel is a multi-variable and multi-parameter nonlinear and discontinuous model optimization problem. It is difficult to solve the classical mathematical analysis model, but with continuing improvements in the current computing power, machine learning (ML) methods provide an effective means of solving such problems. BP neural network is one of the most representative neural network structures in the field of ML methods at present. The BP neural network can store this complex mapping relationship by learning, without knowing the specific mathematical expressions between input and output in advance. The finite element model correction problem is a nonlinear mapping problem between model parameters and structural response values. Therefore, the BP neural network is used as a basis to solve the model correction problem.

2.3.1. Training Data-Set

Training samples have an important impact on the performance of the BP neural network. To train a network with a high-accuracy approximation capability, a sufficient number of samples with distinctive features are necessary. In this way, the trained network generally has a good generalization ability. Let the number of samples of the neural network be N, the total number of weights and thresholds of the neural network be n_w, and the network error accuracy be ε. There is a reasonable corresponding relationship, as follows:

$$N = n_w / \varepsilon \tag{9}$$

A certain disturbance range is applied to the input parameters, and the structural characteristic response is obtained and recorded through the model calculation. Python and the ABAQUS script interface are used for the deep development of finite element software. Automated iterative modeling and parametric analyses are achieved. Based on this, sufficient datasets can be efficiently obtained to train neural networks.

Before training the neural network with the sample set, the samples need to be normalized. X_N represents the original sample, X_N^* represents the normalized sample, and X_{min} and X_{max} represent the minimum and maximum values of the sample, respectively. Considering the presence of displacement data in the sample set used in this paper, and in order not to lose the symbolic features, the samples are normalized using the following equation.

$$X_N^* = \frac{X_N}{\max(|X_{min}||_{max}|} X_N^* \in [-1, 1]) \tag{10}$$

2.3.2. Network Structure Design

In the structural design of the BP neural network, the number of nodes in the hidden layer of the network has a great influence on the performance of the network. If the number of hidden layer nodes is too small, the trained network has a poor mapping ability and low precision. Conversely, an excessive number of nodes will lead to a substantial increase in network training time. This also easily leads to overfitting of the network. After multiple experiments, researchers have derived some empirical formulas as follows.

$$H = \sqrt{I + O} + a \quad a \in [1, 10] \tag{11}$$

$$H = \log_2 I \quad I \in [0.02I, 4I] \tag{12}$$

$$H = \frac{N}{a(I + O)} \quad a \in [2, 10] \tag{13}$$

H is the number of hidden layer nodes. I is the number of input layer nodes. O is the number of output layer nodes. N is the number of training set samples. a is a constant.

2.3.3. Algorithm

The traditional BP neural network algorithm uses the gradient descent algorithm to update the neuron weights and thresholds. When the function that is to be optimized is complex, the gradient descent algorithm is prone to problems of slow convergence and low computational efficiency. The error function of the actual problem is usually not convex, and there are multiple local minimum points. The algorithm may converge to a local minimum, making it difficult to obtain an optimal solution. To improve the problems in the traditional BP neural network training algorithm, the Bayesian regularization (BR) algorithm can be used to accelerate the solution convergence speed.

BR algorithm improves the optimization ability by modifying the performance function of the neural network. The performance function of the algorithm adds weight feedback based on error feedback. The training function of the network is expressed as:

$$F = \alpha E_w + \beta E \tag{14}$$

where E_w is the sum of squares of all network weights. E is the error value between the network output value and the real value of each layer. α and β are the regularization coefficients of the performance function. The value of the coefficient represents the focus of network training. When $\alpha < \beta$, the error of training samples gradually decreases with the increase in training times. When $\alpha > \beta$, the weight gradually decreases with the increase in training times to smooth the network output.

The BR method assumes that the prior probabilities of the training dataset and the weight set obey the Gaussian distribution. The network parameters are adaptively optimized based on the Bayesian criterion. This maximizes the minimum point of the improved

performance function by maximizing the posterior probability of α and β. The method optimizes the performance function by modifying it and adjusting the parameter size during the training process. The algorithm ensures that the prediction accuracy meets the requirements and reduces the network size.

3. Experiments

3.1. Construction and Accuracy Verification of 3D-DIC Measurement System

The camera model was HIKVISION MV-CA050-20GM (Hikvision, Hangzhou, China). The resolution of the camera was 2592 pixel × 2048 pixel. The camera lens model was HIKVISION KF2528M and its focal length was 25 mm. The common field of view of dual cameras was 500 mm × 500 mm. The XL-80 interferometer (Renishaw, Wotton-under-Edge, UK) was used to verify the in-plane and out-of-plane displacement accuracy of the system. The length measurement results of the laser interferometer were used as the relative true value of the displacement measurement. The physical pictures and parameters of the laser interferometer are shown in Table 1.

Table 1. Parameters of RENISHAW XL-80 interferometer.

System accuracy	±0.5 ppm (±0.5 μm/m)
Laser frequency stabilization accuracy	±0.05 ppm (±0.05 μm/m)
Resolution	1 nm
Measuring range	80 m
Maximum measuring speed	4 m/s

The displacement test system is shown in Figure 5. Both the speckle-sprayed specimen and the mirror of the laser interferometer were fixed on the precision stage. The laser interferometer and 3D-DIC system simultaneously monitored the displacement of the test piece. After the precise displacement stage was used to generate displacement during the experiment, the actual displacement of the displacement stage was monitored by a laser interferometer. The 3D-DIC system collected one speckle image of the specimen. The position of the precision stage and the laser interferometer was adjusted. Testing experiments included in-plane and out-of-plane displacements.

(**a**) (**b**)
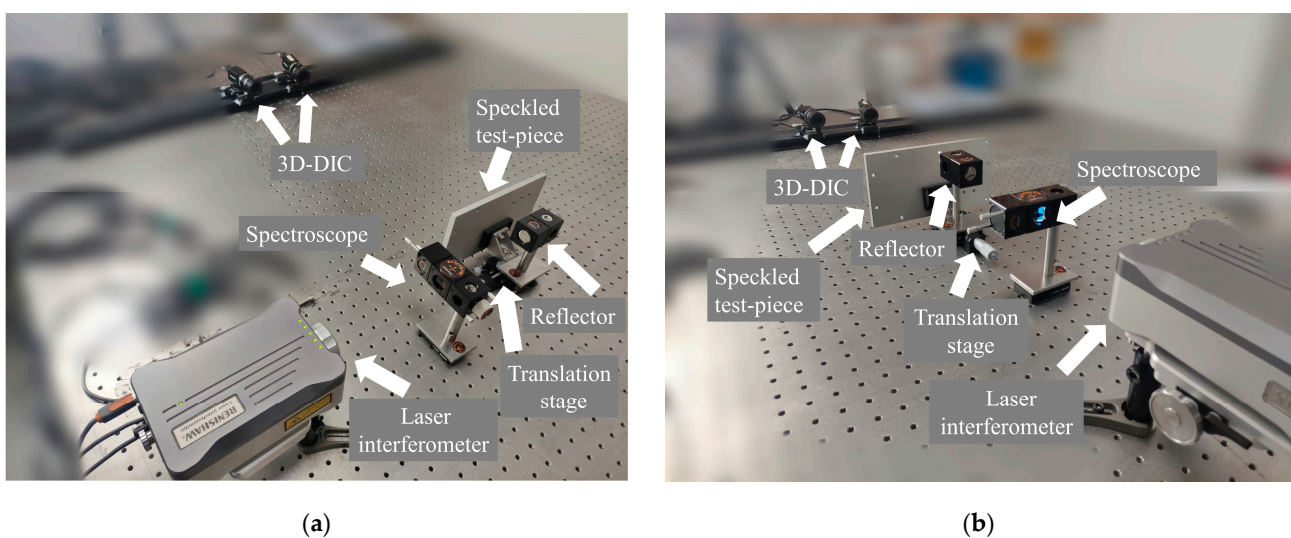
Figure 5. Displacement test system (**a**) in-plane displacement (**b**) out of plane displacement.

The size of the sub-region in the matching calculation affects the measurement accuracy and calculation efficiency. If the sub-area is too small, the influence of noise will increase and the measurement accuracy will be affected. Excessive subregions will lead

to a decrease in spatial resolution and increase the amount of computation. The balance between accuracy and efficiency was fully considered. After many test experiments, a sub-region of 31 pixel × 31 pixel was finally selected for the matching calculation. The test piece was repeatedly moved a certain distance, and the displacement was measured with a laser interferometer and DIC measurement system. In Figure 6, the green polyline represents the displacement data measured by the laser interferometer, and the orange polyline represents the displacement data measured by the DIC measurement system. Taking laser interferometer as the standard, the average error of in-plane displacement measurements by the DIC measurement system is 2.9 μm and the error of out-of-plane displacement measurements is 3.8 μm when comparing the displacement data of the two. The results verify that the 3D-DIC can complete high-precision displacement measurements.

(**a**) (**b**)
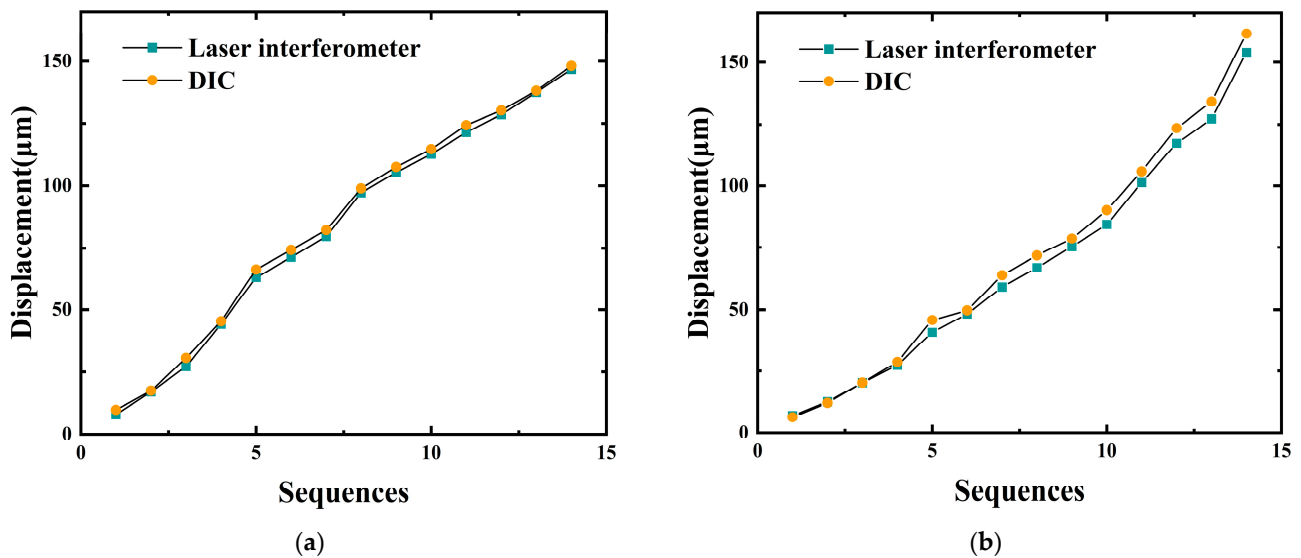
Figure 6. Displacement measurement results (**a**) in-plane displacement (**b**) out-of-plane displacement.

3.2. Measuring System for Honeycomb Panels

The honeycomb structure is composed of three basic materials: honeycomb core, aluminum skin, and adhesive. Honeycomb core material is made of aluminum foil and a special structural adhesive. Structurally, it is composed of three parts: the middle honeycomb core layer, and the upper and lower masks, shown in Figure 7a. In the finite element analysis, the sandwich theory was used to equate the honeycomb core into an anisotropic layer of constant thickness for the equivalent calculation [38]. The honeycomb panel that was tested and its dimensional (840 mm × 640 mm) parameters are shown in Figure 6.

Figure 8 shows the experimental measurement system. The honeycomb sandwich plate was fixed on the measuring frame to simulate the actual assembly state. The honeycomb plate was heated with a heating plate to simulate the high-temperature load. Multiple detection points were evenly arranged on the surface of the honeycomb plate. The temperature of the detection points was measured by a K-type thermocouple.

The experiment measured the three-dimensional deformation of honeycomb panel under multiple working conditions. First, the measurement system collected the surface image of the honeycomb plate when it was not deformed. Then, the honeycomb panel was heated. When the surface temperature field of the honeycomb panel reached a steady state, the surface temperature field was recorded. The measurement system collected deformation images. Finally, the image data collected by the measurement system were processed to obtain the three-dimensional displacement field under the corresponding temperature field. Figure 9 shows the displacement fields in the X, Y and Z directions of the honeycomb sandwich plate when the heating plate was 100 degrees.
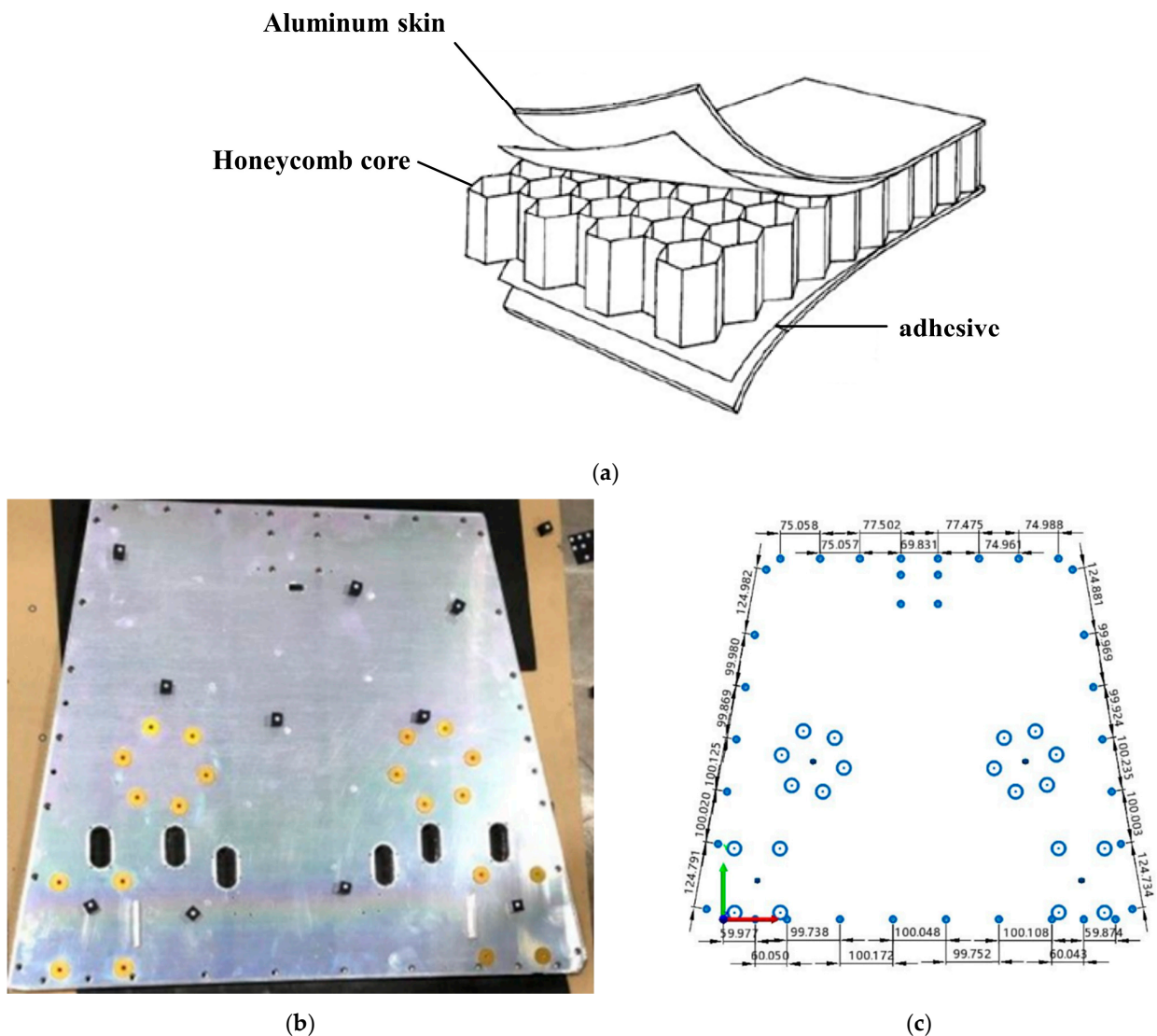
Figure 7. Honeycomb panel and dimensions (**a**) inner structure (**b**) schematic diagram (**c**) physical appearance.

3.3. Finite Element Model Modification Experiment

3.3.1. Establishment of Finite Element Model

The finite element model of the honeycomb sandwich panel was established by ABAQUS software. The geometric model was created according to the actual size parameters. Figure 10 shows the establishment process of the finite element model and the four fixed points of the honeycomb panel. Figure 10a shows the geometric model in the finite element described above. Figure 10b–d shows the finite element model substituted with initial parameters, the four fixed points of the honeycomb panel and the finite element model after meshing, which will be introduced in the following text.

According to the sandwich theory, the model is equivalent to a three-layer structure. The initial material model parameters were calculated using the equivalent calculation method. As shown in Table 2, the material properties of the model were set according to the equivalent parameters, as shown in Figure 10b.

The measured temperature field was mapped to the finite element model to obtain the surface temperature field of the model as the temperature load of the finite element model. Figure 11 shows the temperature distribution field of the honeycomb panel after the heating device heated the central position of the honeycomb panel to 100 degrees Celsius. It can be seen from the figure that the surface temperature of the honeycomb panel was

the highest in the center of the honeycomb panel, and the temperature value gradually decreased around the center.
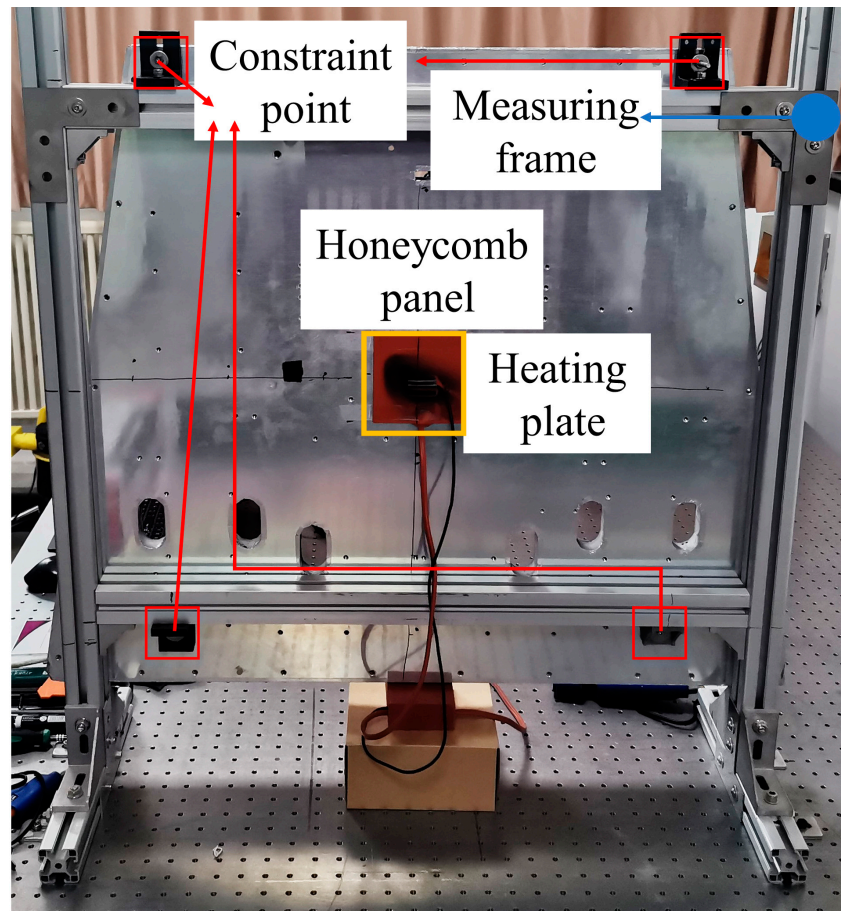
Figure 8. Experimental device diagram.
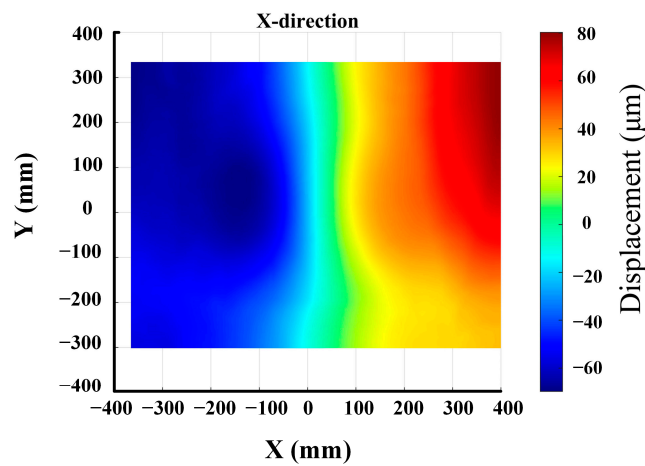
Figure 9. *Cont*.
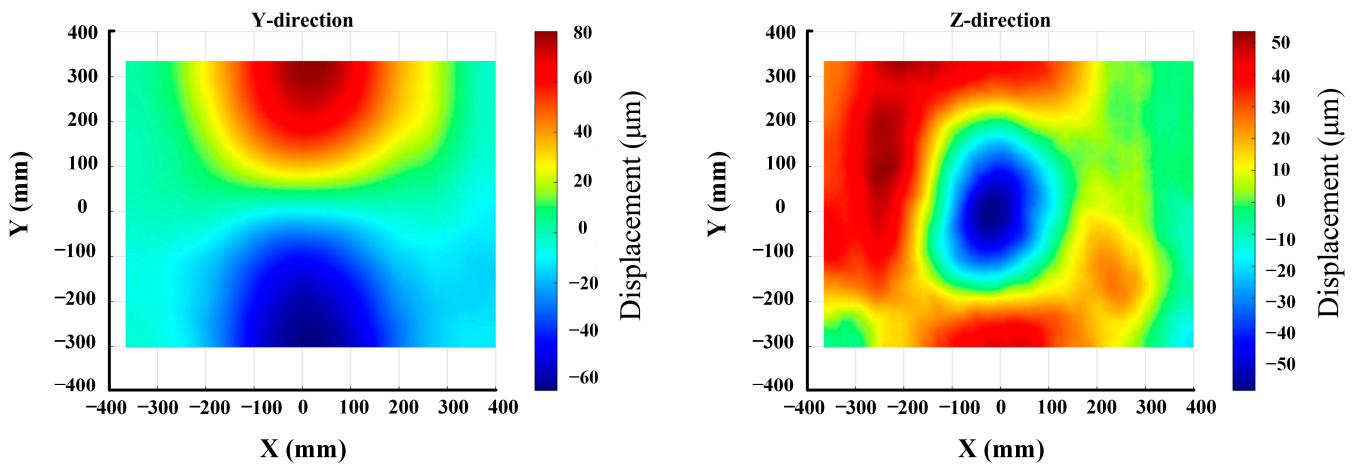
Figure 9. Three-dimensional displacement obtained by the measurement system.
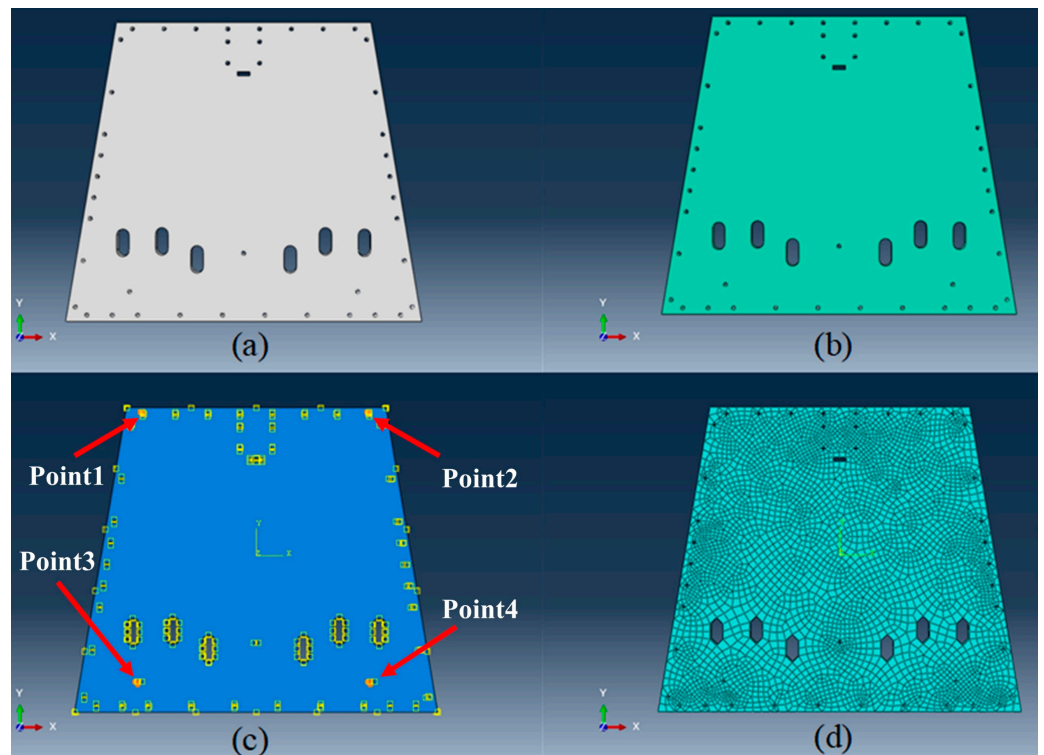
Figure 10. Finite element model of honeycomb panel. (**a**) geometric model (**b**) input material parameters (**c**) fixed points (**d**) divide into hexahedral mesh.

In the finite element simulation model, the constraint of the fixed point on the honeycomb plate could become equivalent to the constraint of the displacement degree of freedom of the corresponding point. Therefore, in the analysis step, the displacement values in the X, Y, and Z directions were given to each fixed point. The fixed points are shown in Figure 10c. The actual measured value was taken as the initial displacement value, as shown in Table 3.

The mesh generation technology of solid elements in ABAQUS mainly includes structured mesh, scanning mesh, and free mesh. In this paper, this was divided into hexahedral (Hex) mesh, and a three-dimensional solid element (C3D8) was used to establish the model. The C3D8 element uses eight nodes to establish the finite element model with stress concentration. The calculation accuracy is very high and the calculation speed of the model is fast. The number of cells in the honeycomb panel model is 18,632 (Figure 10d). After

the initial model was established, the established finite element model was submitted to the ABAQUS solver to obtain the deformation in the honeycomb plate's structure and the displacement field. The displacement values in the X, Y, and Z directions are shown in Figure 12.

Table 2. Model's initial material parameters.

	Parameter		Value
Aluminum skin	Modulus of elasticity		68,000 MPa
	Poisson's ratio		0.36
	Coefficient of expansion		$2.32 \times 10^{-5}/^{\circ}\text{C}$
Honeycomb core	Modulus of elasticity	E1	0.0339 MPa
		E2	0.0339 MPa
		E3	800 MPa
	Poisson's ratio	Nu12	0.33
		Nu13	0
		Nu23	0
	Shear modulus	G12	0.0065 MPa
		G13	45.58 MPa
		G23	68.37 MPa
	Coefficient of expansion		$2.3 \times 10^{-5}/^{\circ}\text{C}$
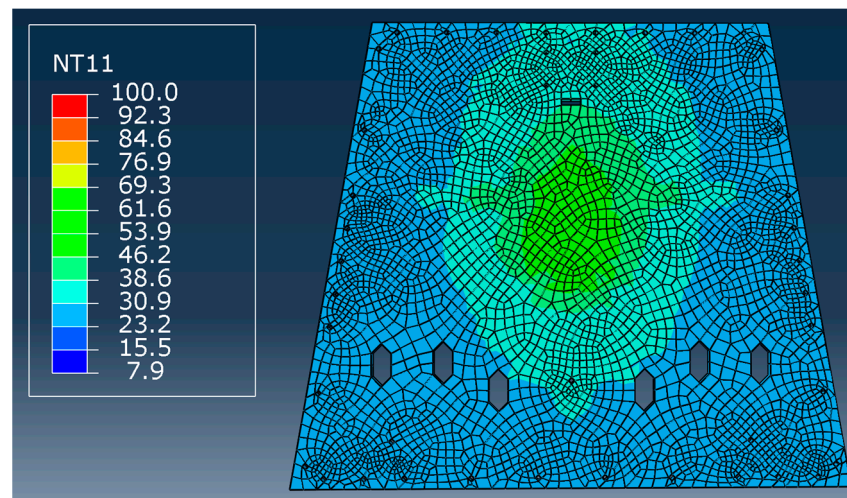
Figure 11. Simulated temperature field (unit: centigrade).

Table 3. Equivalent boundary condition parameters.

Displacement	X/µm	Y/µm	Z/µm
Fixed point 1	−55.26	14.36	37.47
Fixed point 2	62.59	30.01	−12.50
Fixed point 3	−40.77	−2.88	18.73
Fixed point 4	19.27	−10.06	21.36
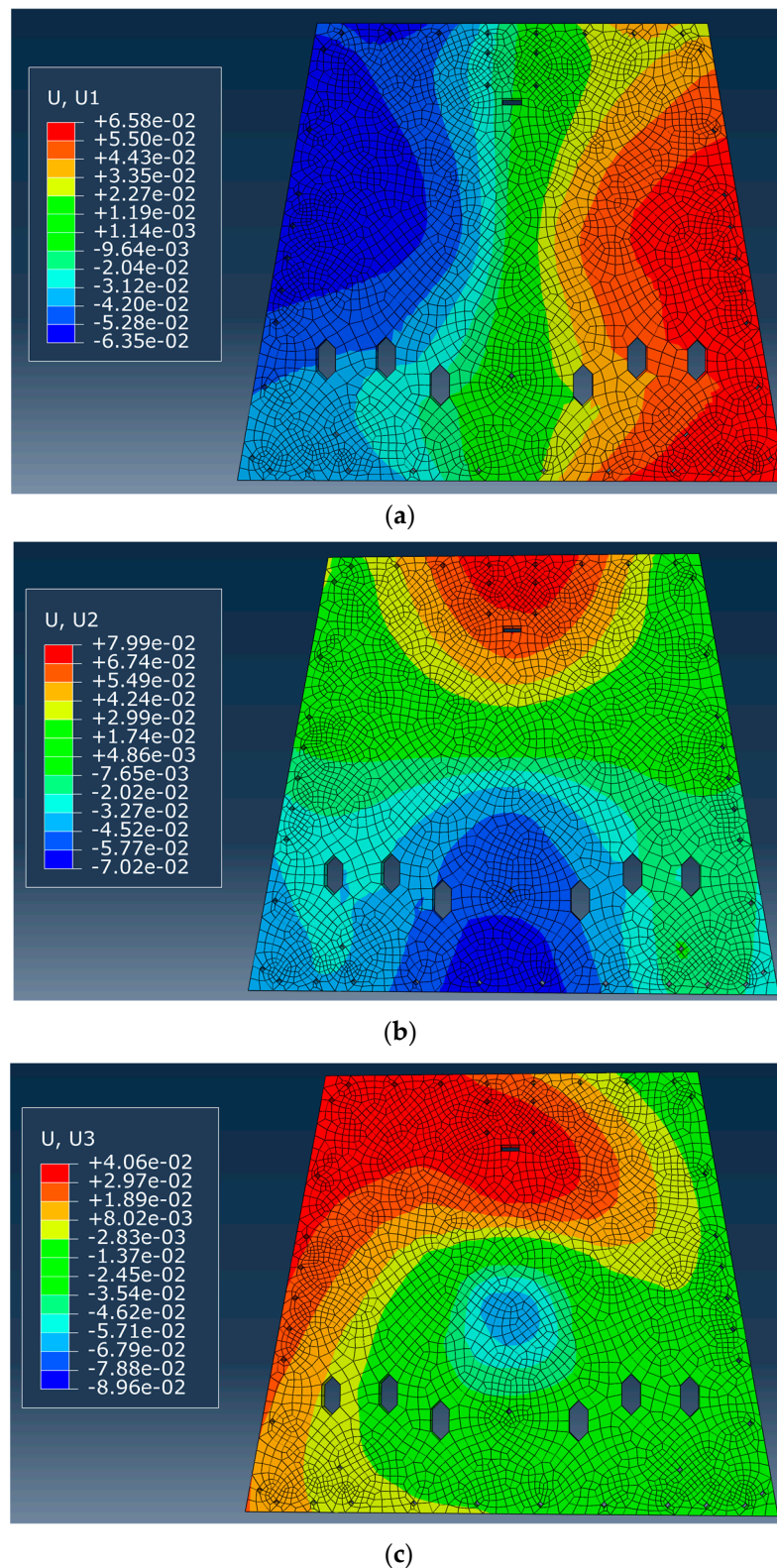
Figure 12. The results of the initial finite element model (unit: mm) (**a**) X-direction (**b**) Y-direction (**c**) Z-direction.

Twelve pre-measured key positions on the surface of the honeycomb panel were selected as calibration points, as shown in Figure 13 and Table 4. Figure 13 marks the position of the calibration point with a red cross. Table 4 shows the specific coordinate data of the calibration point, from the top to the bottom of the picture and from left to right. The

calibration point covered a range of −344.058 mm to 347.026 mm in the X direction and −286.581 mm to 281.114 mm in the Y direction. These points were distributed in four rows, with three points evenly distributed in each row. The finite element model was modified by calibrating these positions. Taking the three-dimensional displacement at the key positions as an example, the error value between the calculated value of the initial finite element model and the actual measured value was compared and analyzed.
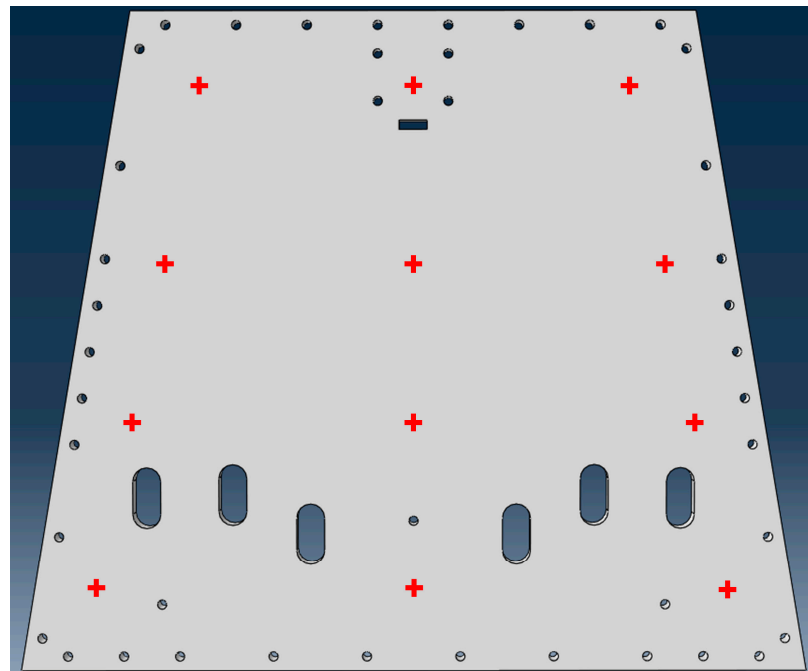
Figure 13. Key positions on the honeycomb panel.

Table 4. X-Y positions of calibration points.

ID	X/mm	Y/mm
Point 1	−278.434	280.106
Point 2	3.143	280.160
Point 3	277.812	281.114
Point 4	−298.643	84.553
Point 5	−1.014	84.093
Point 6	297.361	83.892
Point 7	−323.300	−104.062
Point 8	−2.406	−104.195
Point 9	325.165	−103.593
Point 10	−344.058	−286.581
Point 11	1.602	−284.850
Point 12	347.026	−285.388

As shown in Figure 14, there is a large error between the calculation results of the initial finite element model and the real value. The model cannot accurately reflect the deformation at each position of the honeycomb structural plate.

3.3.2. Establish an Optimization Model

In this experiment, there were 13 material property parameters and 12 equivalent boundary condition parameters of the honeycomb sandwich panel. Sensitivity analysis was performed for all parameters by changing the parameter values of the parameters to be analyzed by 10% relative to each other. The amount of change in the displacement matrix of the honeycomb plate was calculated. Then, the mean value of displacement

was compared with the parameter to obtain the parameter sensitivity. The results of the sensitivity calculations for each parameter are shown in Table 5. The main body in Table 5 shows the 13 material properties of the honeycomb panels. The last column of values represents their sensitivity to the change in displacement value after a 10% change in material properties.
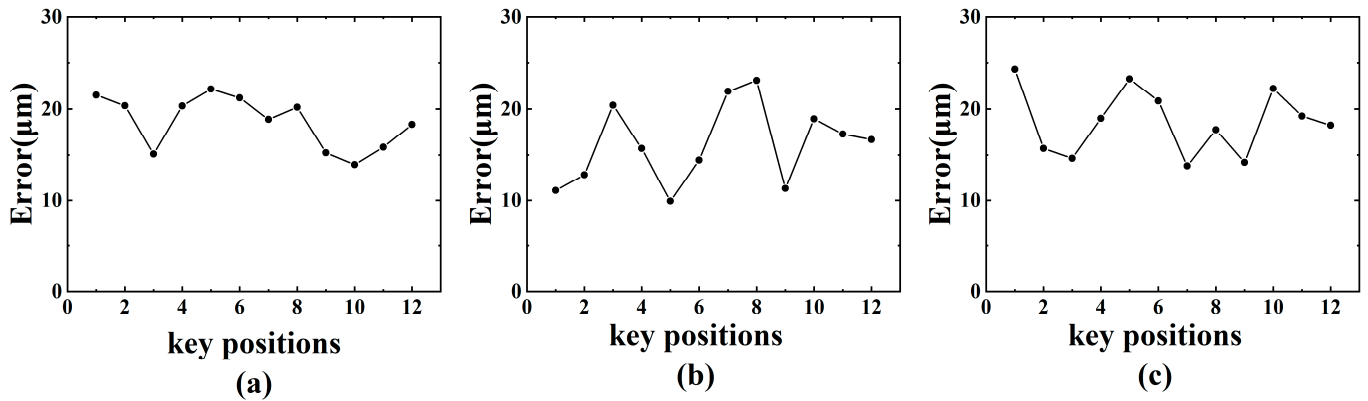
Figure 14. Calculation error of initial model at key positions (**a**) X-direction (**b**) Y-direction (**c**) Z-direction.

Table 5. Parameter sensitivity analysis results.

Parameter			Sensitivity
Aluminum skin	Modulus of elasticity		6.00×10^{-5}
	Poisson's ratio		7.78×10^{-4}
	Coefficient of expansion		4.5×10^{-3}
Honeycomb core	Modulus of elasticity	E1	1.65×10^{-8}
		E2	2.32×10^{-8}
		E3	2.88×10^{-6}
	Poisson's ratio	Nu12	1.04×10^{-8}
		Nu13	-
		Nu23	-
	Shear modulus	G12	8.01×10^{-9}
		G13	5.41×10^{-5}
		G23	5.17×10^{-5}
	Coefficient of expansion		2.29×10^{-4}

By analyzing the parameters in Table 5, parameters with a sensitivity lower than 10^{-4} have were shown to have few errors in their results. In the case of a ±10% variation in these parameters, the effect on the results is less than 0.1 μm. Therefore, only the expansion coefficient of skin, Poisson's ratio and expansion coefficient of honeycomb core were considered in the finite element model modification process. Table 6 summarizes the variables that were subsequently used to modify the finite element model, including 3 material properties and 12 boundary conditions. A total of 15 variables were used as the output parameters of the neural network.

Table 6. Parameters of model correction.

Material property parameters	Skin expansion coefficient, Poisson's ratio, honeycomb core expansion coefficient
Boundary condition parameters	Displacement parameters of fixed points 1–4

3.3.3. Training BP Neural Network

In this section, a Python script was written for the secondary development of the ABAQUS script interface. The established finite element model was parametrically analyzed, and the software automatically obtained 1000 sets of neural network training samples. According to the actual measured parameter values, the parameter disturbance range can be determined, as shown in Table 7. There was no need to repeatedly build and process models for each parametric analysis process; it was only necessary to modify the corresponding parameters and add random disturbance. Then, the finite element model was solved to obtain the structural response value. Finally, the three-dimensional displacement values of these key positions were obtained.

Table 7. Range of parameter disturbance.

Parameter	Range of Disturbance
Coefficient of skin expansion	$\pm 0.02 \times 10^{-5}/°C$
Poisson's ratio of skin expansion	± 0.02
The expansion coefficient of the honeycomb core	$\pm 0.02 \times 10^{-5}/°C$
Displacement of fixed points	$\pm 20\ \mu m$

In the experiment, the BP neural network contained a hidden layer. The number of neurons in the input layer of the network was 36, which were the X, Y, and Z displacement values of 12 calibration points. The number of neurons in the output layer was 15, which was the correction parameter of the finite element model. It is necessary to study the number of neurons in the hidden layer. According to the estimation formula, the value range of hidden layer nodes is 1~25. The number of hidden layer nodes were adjusted within this range to build a neural network. The neural network was trained with the training samples obtained from the parametric analysis. The root mean squared error (MSE) of the training and test sets was obtained.

The overfitting degree is characterized by the ratio of the network error in the test set and the error of the training set. Figure 15 shows how to determine the number of hidden nodes in the neural network based on the training set and test set. The blue curve in Figure 15 shows the MSE results of the neural network on the training set. The green curve represents the MSE results of the neural network on the test set. The orange curve shows the ratio of the first two values, which is used to indicate the degree of overfitting in the neural network. When the value of the orange curve exceeds 100%, the greater the value, the higher the degree of overfitting. The criterion formula for setting the number of hidden nodes of the neural network is given in Section 2.3.2. Through calculation, it can be shown that the appropriate number of hidden nodes is 8–11. The blue curve in Figure 15 is the MSE result of the neural network on the training set, the green curve is the MSE result of the neural network on the test set, and the yellow curve represents the overfitting of the neural network during the training process. As shown in Figure 15, with the increase in the number of hidden layer nodes, the error in the training set and the error in the test set are significantly reduced. The degree of overfitting gradually becomes obvious; that is, the network performed well in the training set and showed a large error in the test set. Considering the network accuracy and generalization ability, the optimal number of hidden layer nodes is 10.

The network parameters selected in the experiment are shown in Table 8. The network converged after 53 epochs of iterative training, as shown in Figure 16. The blue curve in Figure 16 is the MSE result curve when the neural network is iteratively trained on the training set. The green curve is the MSE result curve when the neural network is iteratively trained on the verification set. The red curve is the MSE result curve when the neural network is iteratively trained on the test set. The dotted line is the minimum error of the neural network during iterative training. The MSE of the results is 1.02×10^{-8}. The magnitude of the error is small, meaning that the network meets the design requirements.

The network accuracy can be determined by the correlation coefficient R. The calculation formula of the correlation coefficient is:

$$R = \sqrt{1 - E} \tag{15}$$
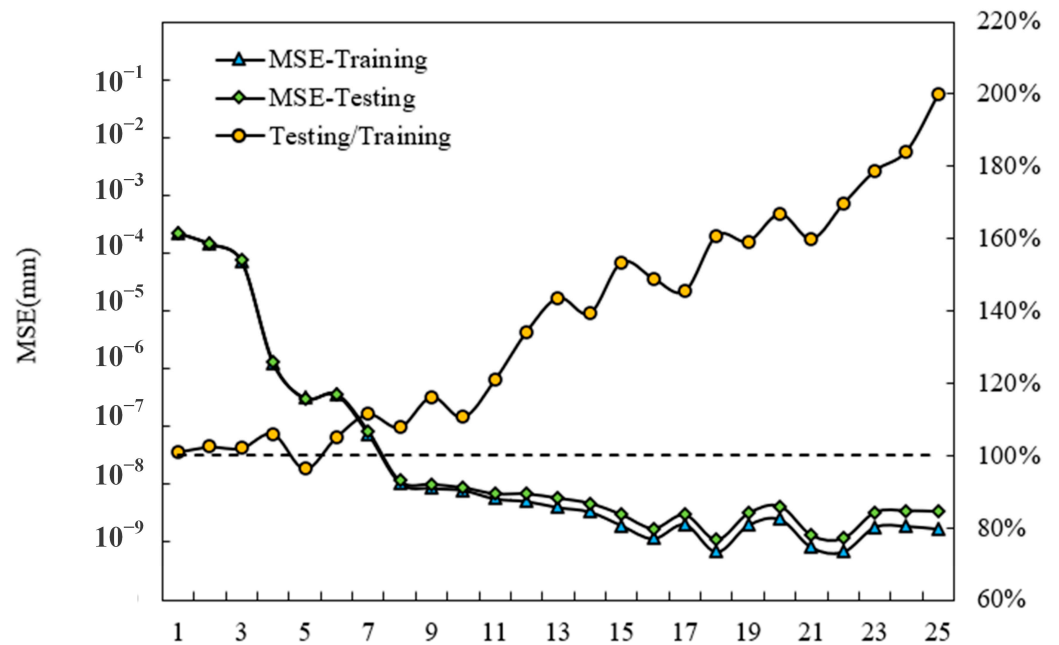
Figure 15. The network error and overfitting analysis.

Table 8. Network parameters.

Number of Neurons in the Hidden Layer	The Hidden Layer Response Function	Output Layer Response Function	Optimization Function	Gradient Threshold ε	Error Function
10	tansig	purelin	BR	1×10^{-7}	MSE

E is the average relative error. The accuracy of the BP neural network model is r = 0.9997. The larger the correlation coefficient, the better the model effect. Figure 17 shows the predicted correlation coefficients of the network on the training set, test set, and all samples. The regression value R represents the correlation between the predicted output and the target output. The closer the R value is to 1, the closer the relationship between prediction and output data; the closer the R value is to 0, the greater the randomness of the relationship between prediction and output data. The abscissa represents the target output, and the ordinate represents the fitting function between the predicted output and the target output. The figure shows that the data correlation of training set, test set and overall results after neural network training is 0.99965, 0.99996 and 0.9997, respectively.

Based on previous experiments, the three-dimensional displacement data measured for key positions were used as input parameters in the trained BP neural network. From this, the modified finite element model parameters were obtained, as shown in Table 9.

The parameters of the finite element model were substituted into the established finite element model to obtain the modified finite element model and calculate the displacement field. The results are shown in Figure 18. The change from blue to red in Figure 18 shows the change in displacement value. The specific changes in displacement values in the figure are almost consistent with the displacement results of the previous DIC measurement system. It can be seen that the correction of the finite element model is excellent.
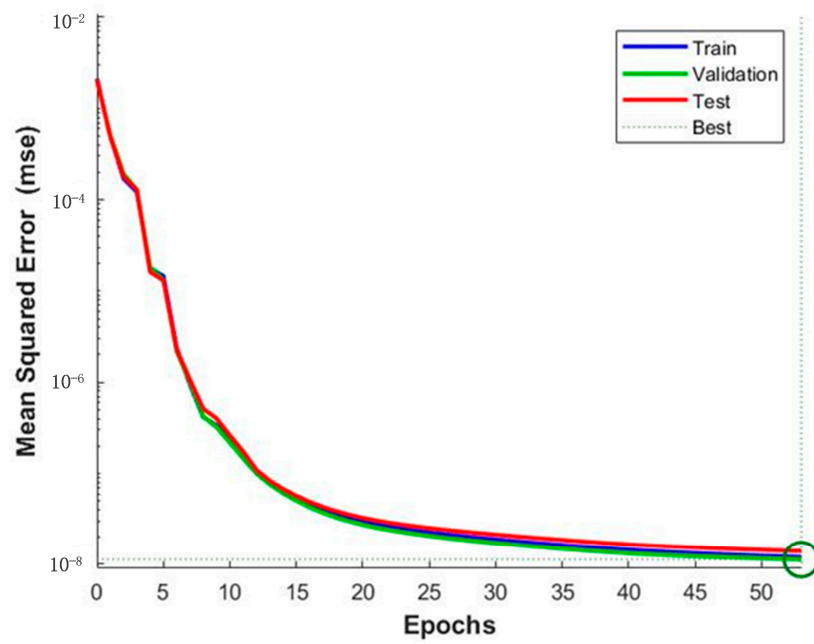
Figure 16. MSE of the network.
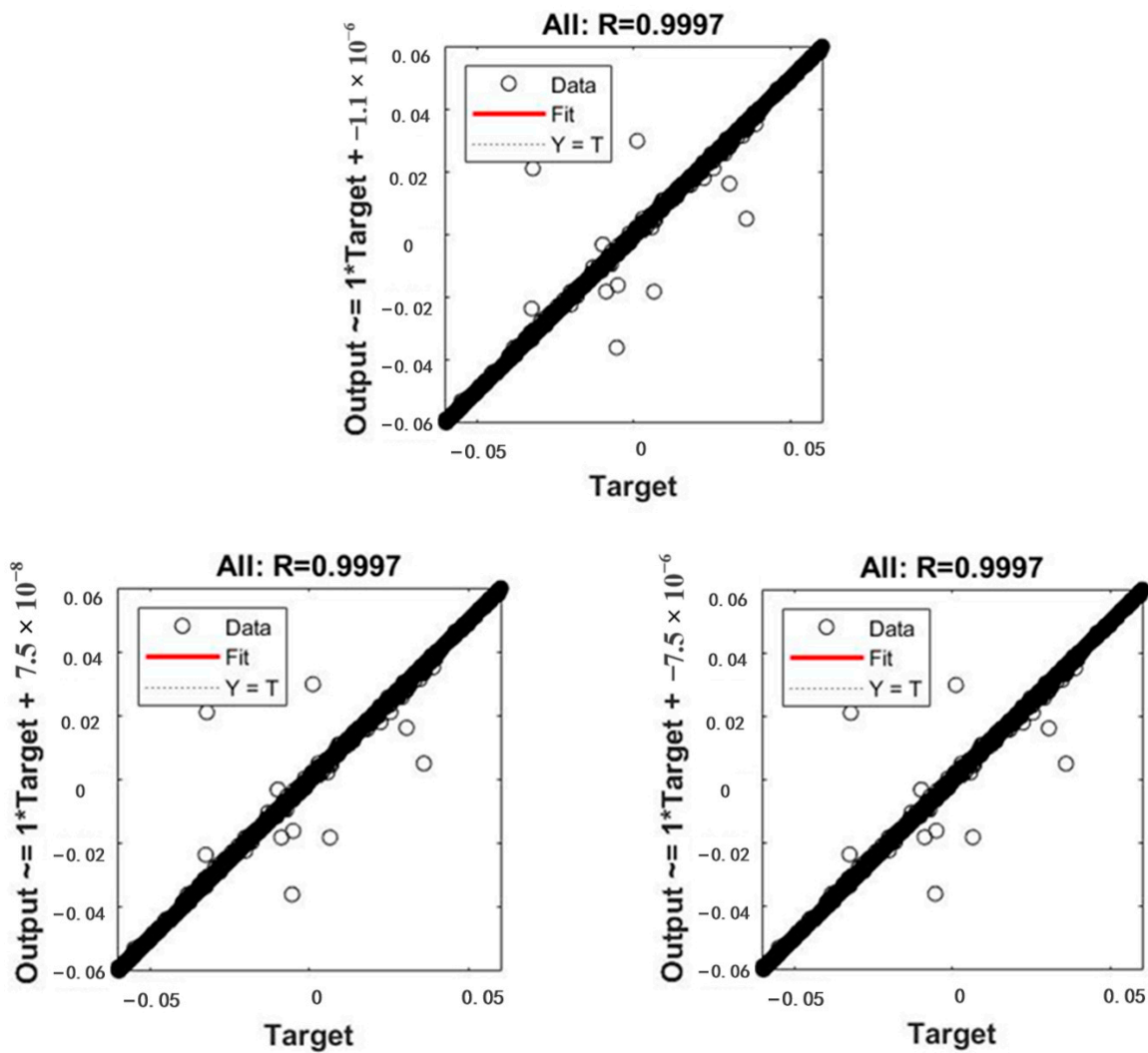
Figure 17. The *R* value of the network.

Table 9. Modified finite element model parameters.

Parameter		Value
The expansion coefficient of skin		$2.33 \times 10^{-5}/°C$
Poisson's ratio of skin		0.362
The expansion coefficient of the honeycomb core		$2.30 \times 10^{-5}/°C$
Displacement parameters of fixed point 1	X-direction	-62.03 μm
	Y-direction	1.60 μm
	Z-direction	37.22 μm
Displacement parameters of fixed point 2	X-direction	70.15 μm
	Y-direction	11.36 μm
	Z-direction	-27.54 μm
Displacement parameters of fixed point 3	X-direction	-39.98 μm
	Y-direction	-0.61 μm
	Z-direction	35.66 μm
Displacement parameters of fixed point 4	X-direction	28.70 μm
	Y-direction	-7.73 μm
	Z-direction	36.85 μm

(**a**)

(**b**)

Figure 18. *Cont*.

(**c**)
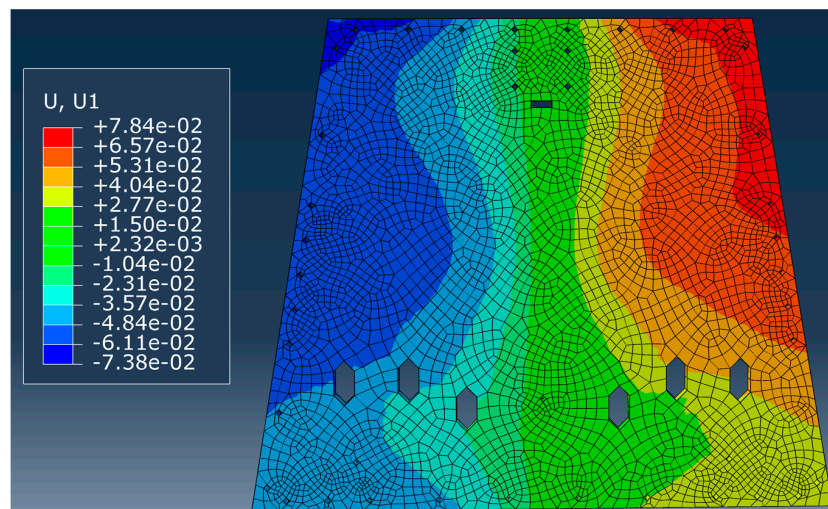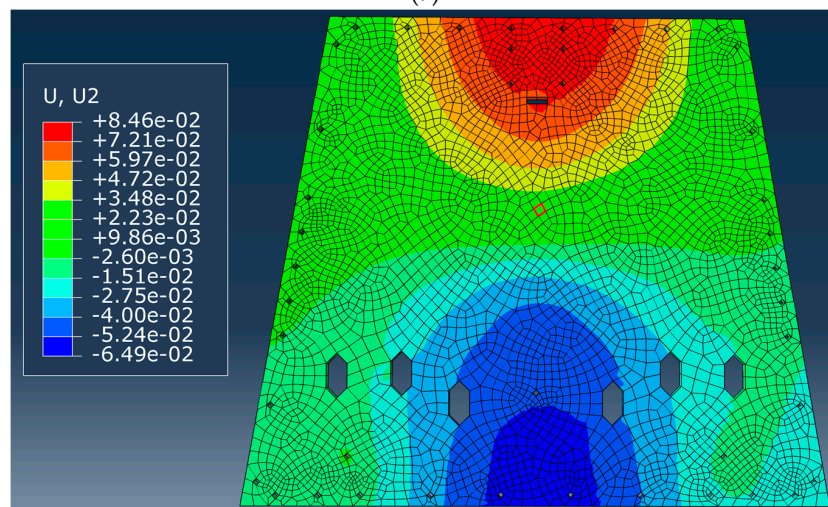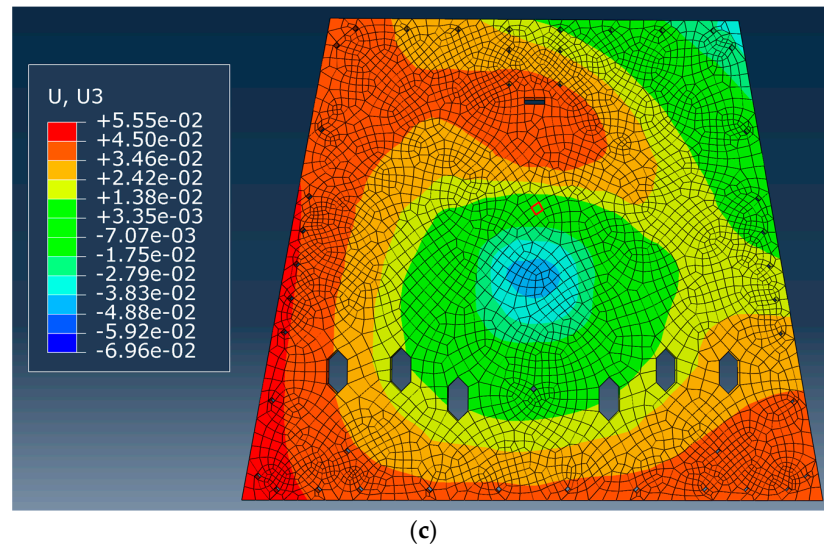
Figure 18. Calculation results of the modified finite element model (unit: mm) (**a**) X-direction (**b**) Y-direction (**c**) Z-direction.

In the experiment, the actual 3D-DIC measured value is the true value compared with the displacement at the key positions. The errors before and after model correction are shown in Figure 19. The orange curve in Figure 19 represents the displacement measurement error of the initial finite element model at the calibration point, and the blue curve represents the displacement measurement error of the modified finite element model at the same location. The error in the initial finite element model ranged from 10 μm to 30 μm, while the error range of the modified finite element model was maintained below 10 μm. The results show that these key positions can be used as calibration points to successfully modify the finite element model.
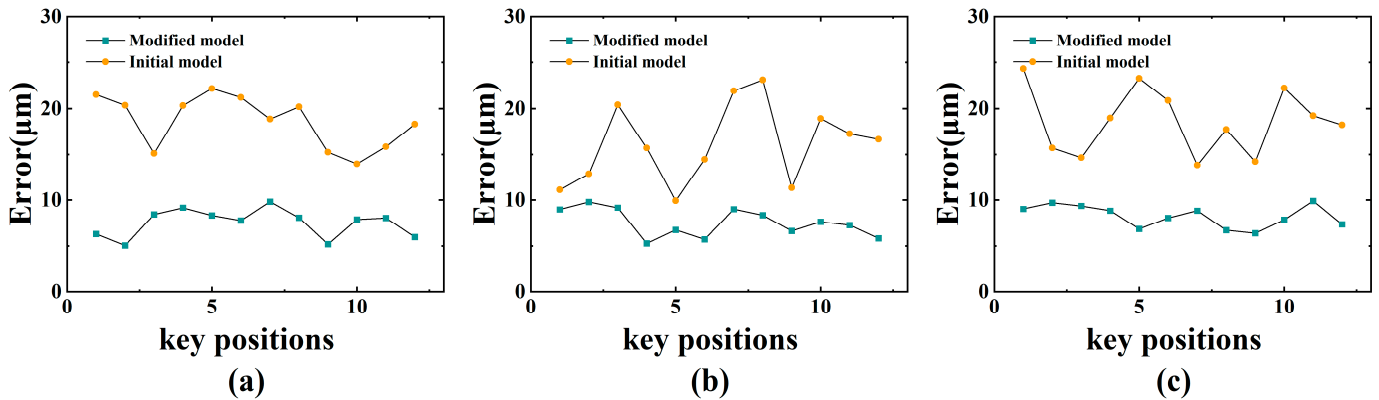
Figure 19. Comparison of calculation errors before and after finite element model correction at key positions (**a**) X-direction (**b**) Y-direction (**c**) Z-direction.

To verify the accuracy of the modified finite element model, 18 feature points on the surface of the honeycomb panel were selected as measurement points. This is shown in Figure 20. The red cross in Figure 20 indicates the coordinate position of the measuring point. All points were divided into four lines, with four points distributed in the upper two lines and five points distributed in the lower two lines. The finite element model that was corrected with the calibration point was used to compare the simulation value of the finite element model at the feature point with the actual value measured by the DIC measurement system. Figure 21 shows the displacement measurement error of the initial finite element model and the modified finite element model at the selected measurement points. The orange curve in the figure represents the initial finite element model data, and

the blue curve represents the revised finite element model data. The errors in the initial finite element model ranged from 10 μm to 30 μm, and the error range of the modified finite element model was below 10 μm. The results shown in Figure 21 reveal that the error in the corrected finite element model was significantly reduced, and the model correction effect was remarkable. This proves the feasibility of the finite element correction method based on the BP neural network.
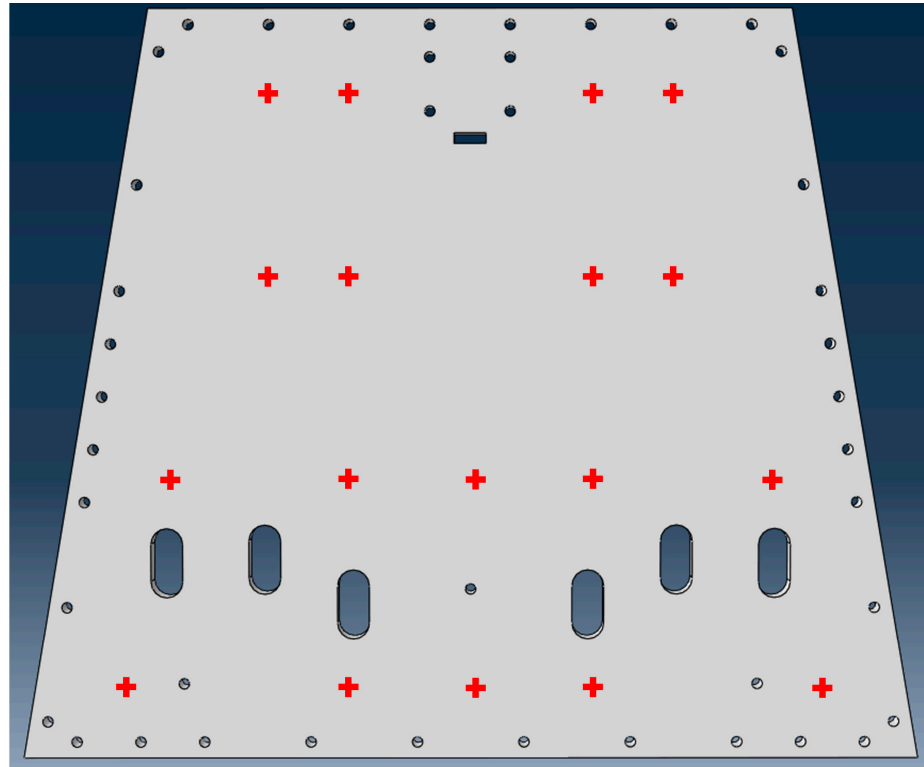
Figure 20. Schematic diagram of surface feature points.
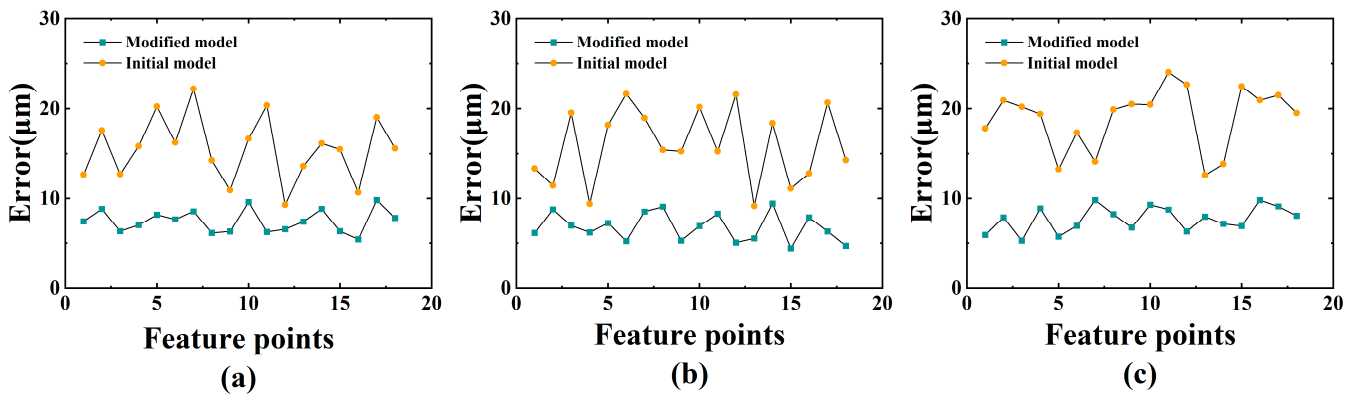
Figure 21. Comparison of calculation errors before and after finite element model correction at feature points (**a**) X-direction (**b**) Y-direction (**c**) Z-direction.

3.4. Accuracy Analysis of Deformation Prediction

The deformation of the honeycomb structural plate is also different under different temperature loads. Based on this, the parameters of the finite element model were further optimized. The above model correction process was repeated, and the temperature load was set at 60 °C, 80 °C, and 100 °C, respectively. The correction parameters under different temperature loads were obtained according to the measured deformation results. According to the least square method, polynomial fitting was carried out for multiple groups of

model parameters to obtain the model correction parameters under the on-orbit simulation temperature, as shown in Table 10. The parameters shown in Table 10 are the final modified finite element model parameters. By writing these parameters into the finite element model, the finite element model can accurately monitor the displacement of the honeycomb panel within the set temperature range.

Table 10. Model correction parameters under in-orbit simulation temperature.

Parameter		Value
The expansion coefficient of skin		$2.33 \times 10^{-5}/°C$
Poisson's ratio of skin		0.362
The expansion coefficient of the honeycomb core		$2.30 \times 10^{-5}/°C$
Displacement parameters of fixed point 1	X-direction	-34.59 μm
	Y-direction	1.36 μm
	Z-direction	21.45 μm
Displacement parameters of fixed point 2	X-direction	36.32 μm
	Y-direction	7.91 μm
	Z-direction	-16.52 μm
Displacement parameters of fixed point 3	X-direction	-20.77 μm
	Y-direction	-0.34 μm
	Z-direction	14.76 μm
Displacement parameters of fixed point 4	X-direction	13.79 μm
	Y-direction	-3.36 μm
	Z-direction	25.45 μm

By substituting the parameters in the table into the finite element model, the error between the corrected value of the model and the measured true value at 70 °C and 90 °C is shown in Figure 22. The curve in Figure 22 shows a displacement value comparison between the modified finite element model and the DIC measurement system to obtain the error in the finite element model during displacement measurements. The results show that the modified finite element model can predict the deformation of the honeycomb structure under a simulated temperature field with high accuracy of better than 10um. The results meet the requirements of high-precision prediction, which also verifies the reliability of the proposed method. When it is difficult to carry out actual measurement, the deformation of the satellite structure in the orbit environment can be predicted with high precision according to the finite element model.

(a)
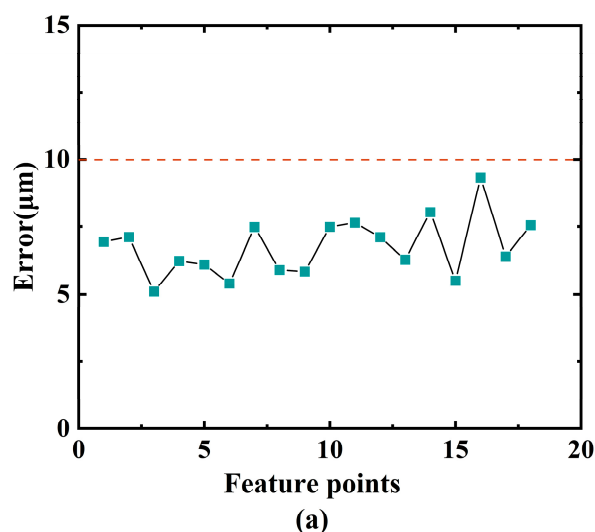
Figure 22. *Cont*.
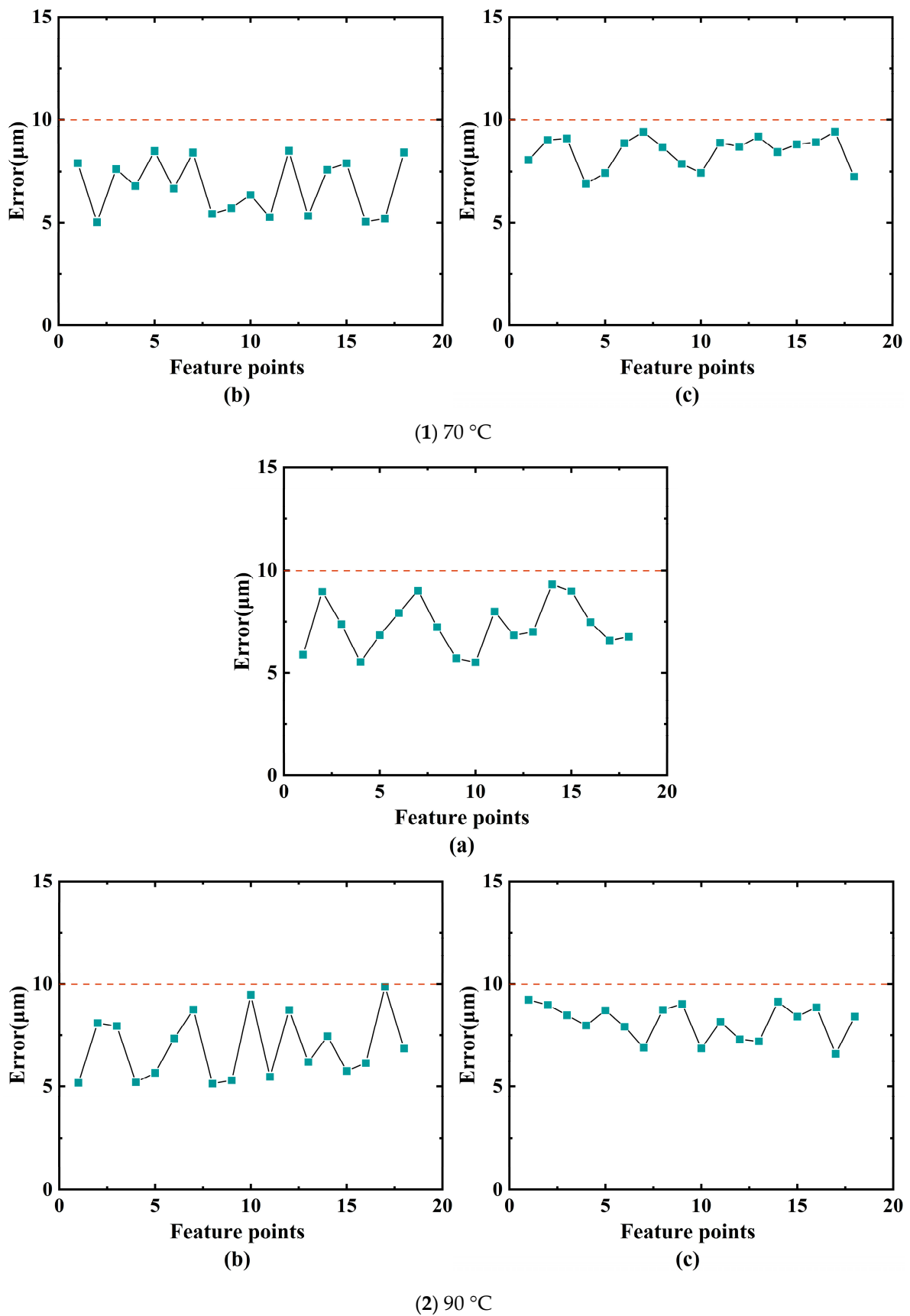
Figure 22. Deformation prediction accuracy of finite element model at feature points under (**1**) 70 °C and (**2**) 90 °C (**a**) X-direction (**b**) Y-direction (**c**) Z-direction.

4. Conclusions

　　Focusing on the problem of high-precision deformation measurements at key satellite structures in the space environment, this paper proposes a new measurement method that fuses physical measurement with FEM models, which can remove the limitations of existing pure measurement methods. The idea of a hybrid physical computational measurement is introduced and fully verified. The 3D digital correlation method is used to obtain the high-precision deformation in the honeycomb panel in a ground simulation environment. Through the trained neural network, high-precision deformation data are used to modify the finite element model. After the finite element model is modified, multiple physical parameters, such as deformation and temperature, are correlated. The large-scale thermal deformation of the in-orbit satellite can be predicted using the temperature data of the in-orbit satellite. The testing results show that the prediction accuracy of the model under different temperature loads can be controlled within 10 μm at the 840 mm × 640 mm scale. This shows that a high predictive accuracy can be received when using the revised model for the complete deformation of large structural parts, suggesting a great application value in the fields of satellite, aircraft, and other large-scale manufacturing.

Author Contributions: Conceptualization, L.Y.; methodology L.Y. and Z.F.; validation Z.F. and K.W.; resources H.S.; formal analysis S.H.; writing—original draft preparation, L.Y. and Z.F.; writing—review and editing, L.Y.; supervision, J.Z. All authors have read and agreed to the published version of the manuscript.

Funding: National Natural Science Foundation of China (Grant Nos. 51975408, 52127810, 51721003).

Institutional Review Board Statement: Not applicable.

Informed Consent Statement: Not applicable.

Data Availability Statement: Not applicable.

Conflicts of Interest: The authors declare no conflict of interest.

References

1.　Horst, S.; Chrone, J.; Deacon, S.; Le, C.; Maillard, A.; Molthan, A.; Nguyen, A.; Osmanoglu, B.; Oveisgharan, S.; Perrine, M.; et al. NASA's Surface Deformation and Change Mission Study. In Proceedings of the 2021 IEEE Aerospace Conference, Big Sky, MT, USA, 6–13 March 2021; pp. 1–19.

2.　Corbacho, V.V.; Kuiper, H.; Gill, E. Review on thermal and mechanical challenges in the development of deployable space optics. *J. Astron. Telesc. Instrum. Syst.* **2020**, *6*, 010902.

3.　Le, V.T.; San Ha, N.; Goo, N.S. Advanced sandwich structures for thermal protection systems in hypersonic vehicles: A review. *Compos. Part B Eng.* **2021**, *226*, 109301. [CrossRef]

4.　Ji, L.; Wang, H. Analysis of On-orbit Thermal Deformation of Flexible SAR Antenna. In Proceedings of the 2021 2nd China International SAR Symposium (CISS), Shanghai, China, 3–5 November 2021; pp. 1–6.

5.　He, Y.; Li, B.; Wang, Z.; Zhang, Y. Thermal Design and Verification of Spherical Scientific Satellite Q-SAT. *Int. J. Aerosp. Eng.* **2021**, *2021*, 9961432. [CrossRef]

6.　Shen, Z.; Li, H.; Liu, X.; Hu, G. Thermal-structural dynamic analysis of a satellite antenna with the cable-network and hoop-truss supports. *J. Therm. Stress.* **2019**, *42*, 1339–1356. [CrossRef]

7.　Zhang, H.; Zhao, X.; Mei, Q.; Wang, Y.; Song, S.; Yu, F. On-orbit thermal deformation prediction for a high-resolution satellite camera. *Appl. Therm. Eng.* **2021**, *195*, 117152. [CrossRef]

8.　Li, J.; Yan, S. Thermally induced vibration of the composite solar array with honeycomb panels in low earth orbit. *Appl. Therm. Eng.* **2014**, *71*, 419–432. [CrossRef]

9.　He, M.; Hu, W. A study on composite honeycomb sandwich panel structure. *Mater. Des.* **2008**, *29*, 709–713. [CrossRef]

10.　Seo, S.I.; Kim, J.S.; Cho, S.H.; Kim, S.C. Manufacturing and Mechanical Properties of a Honeycomb Sandwich Panel. *Mater. Sci. Forum* **2008**, *580–582*, 85–88. [CrossRef]

11.　Wu, M.; Liu, J. Study on Thermal Performance of Single-layer and Multi-layer Stone Aluminum Honeycomb Composite Panels. *J. Phys. Conf. Ser.* **2019**, *1300*, 012002. [CrossRef]

12.　Amini, A.; Mohammadimehr, M.; Faraji, A.R. Active control to reduce the vibration amplitude of the solar honeycomb sandwich panels with CNTRC facesheets using piezoelectric patch sensor and actuator. *Steel Compos. Struct.* **2019**, *32*, 671–686.

13. Ibrahim, S.K.; Mccue, R.; O'Dowd, J.A.; Farnan, M.; Karabacak, D.M. Fiber sensing for space applications. In Proceedings of the European Conference on Spacecraft Structures Materials and Environmental Testing (ECSSMET 2018), Noordwijk, The Netherlands, 28 May–1 June 2018.

14. Aqueeb, A.; Yang, M.; Braaten, B.; Burczek, E.; Roy, S. A Real-Time and Wireless Structural Health Monitoring Scheme for Aerospace Structures Using Fibre Bragg Grating Principle. In *Photonics, Plasmonics and Information Optics*; CRC Press: Boca Raton, FL, USA, 2021; pp. 241–266.

15. Wang, X.; Gao, Z.; Yang, S.; Gao, C.; Sun, X.; Wen, X.; Feng, Z.; Wang, S.; Fan, Y. Application of digital shearing speckle pattern interferometry for thermal stress. *Measurement* **2018**, *125*, 11–18. [CrossRef]

16. Shrestha, R.; Kim, W. Non-destructive testing and evaluation of materials using active thermography and enhancement of signal to noise ratio through data fusion. *Infrared Phys. Technol.* **2018**, *94*, 78–84. [CrossRef]

17. Wang, B.; Zhong, S.; Lee, T.-L.; Fancey, K.S.; Mi, J. Non-destructive testing and evaluation of composite materials/structures: A state-of-the-art review. *Adv. Mech. Eng.* **2020**, *12*, 1687814020913761. [CrossRef]

18. Kudela, P.; Wandowski, T.; Malinowski, P.; Ostachowicz, W. Application of scanning laser Doppler vibrometry for delamination detection in composite structures. *Opt. Lasers Eng.* **2016**, *99*, 46–57. [CrossRef]

19. Liu, G.; Jianhua, R.; Luo, W. Research on Thermal Deformation Analysis and Test Verification Method for Spacecraft High-stability Structure. *Spacecr. Eng.* **2014**, *23*, 64–70.

20. Jiang, S.; Yang, L.; Xu, J.; Yu, J. Deformation measurement for satellite antenna by close-range photogrammetry. In Proceedings of the SPIE—The International Society for Optical Engineering, San Diego, CA, USA, 25–29 August 2013; p. 8896.

21. Blanchard, A.; Kosmatov, N.; Loulergue, F. A Lesson on Verification of IoT Software with Frama-C. In Proceedings of the 2018 International Conference on High Performance Computing & Simulation, Orléans, France, 16–20 July 2018.

22. De Angelis, G.; Meo, M.; Almond, D.P. A new technique to detect defect size and depth in composite structures using digital shearography and unconstrained optimization. *NDT E Int. Indep. Nondestruct. Test. Eval.* **2012**, *45*, 91–96. [CrossRef]

23. Yumuş, C.; Atici, G.; Duman, C. Thermomechanical Design and Analysis of Waveguides on Communication Satellite Payloads. In Proceedings of the 2019 9th International Conference on Recent Advances in Space Technologies (RAST), Istanbul, Turkey, 11–14 June 2019; pp. 363–367.

24. Qian, Z.; Luo, W.; Yin, Y.; Zhang, L.; Bai, G.; Cai, Z.; Fu, W.; Lu, Q.; Zhang, X.; Zhao, C. Dimensional stability design and verification of GF-7 satellite structure. *Chin. Space Sci. Technol.* **2020**, *40*, 10.

25. Mao, J.; Zhang, W.H. Engineering Applications of Satellite Structural Optimization Utilizing ANSYS/CATIA. *Appl. Mech. Mater.* **2012**, *110–116*, 1567–1575. [CrossRef]

26. Güvenç, C.; Topcu, B.; Tola, C. Mechanical design and finite element analysis of a 3 unit cubesat structure. *Mach. Technol. Mater.* **2018**, *12*, 193–196.

27. Halloin, H.; Jeannin, O.; Argence, B.; Bourrier, V.; De Vismes, E.; Prat, P. Lisa on table: An optical simulator for lisa. In Proceedings of the International Conference on Space Optics 2010, Rhodes Island, Greece, 4–8 October 2010; Society of Photo-Optical Instrumentation Engineers (SPIE) Conference Series; SPIE: Washington, DC, USA, 2017. [CrossRef]

28. Kovács, R.; Józsa, V. Thermal analysis of the SMOG-1 PocketQube satellite. *Appl. Therm. Eng.* **2018**, *139*, 506–513. [CrossRef]

29. Ca Lvi, A. An Overview of the E.C.S.S. In *Handbook for Spacecraft Loads Analysis, Proceedings of the III ECCOMAS Thematic Conference on Computational Methods in Structural Dynamics and Earthquake Engineering, Corfu, Greece, 12–14 June 2013*; ECCOMAS: Barcelona, Spain, 2014; Available online: https://www.eccomasproceedia.org/conferences/thematic-conferences/compdyn-2013 (accessed on 15 November 2022).

30. Owens, A.T.; Tippur, H.V. Measurement of mixed-mode fracture characteristics of an epoxy-based adhesive using a hybrid digital image correlation (DIC) and finite elements (FE) approach. *Opt. Lasers Eng.* **2021**, *140*, 106544. [CrossRef]

31. Balcaen, R.; Wittevrongel, L.; Reu, P.L.; Lava, P.; Debruyne, D. Stereo-DIC calibration and speckle image generator based on FE formulations. *Exp. Mech.* **2017**, *57*, 703–718. [CrossRef]

32. Siddiqui, M.Z. 2D-DIC for the quantitative validation of FE simulations and non-destructive inspection of aft end debonds in solid propellant grains. *Aerosp. Sci. Technol.* **2014**, *39*, 128–136. [CrossRef]

33. Babaeeian, M.; Mohammadimehr, M. Investigation of the time elapsed effect on residual stress measurement in a composite plate by DIC method. *Opt. Lasers Eng.* **2020**, *128*, 106002. [CrossRef]

34. Ross-Pinnock, D.; Yang, B.; Maropoulos, P.G. Integration of Thermal and Dimensional Measurement—A Hybrid Computational and Physical Measurement Method. In Proceedings of the 38th International MATADOR Conference, Huwei, Taiwan, 28–31 March 2015; Springer: Cham, Switzerland, 2022; pp. 627–639.

35. De Chiffre, L.; González-Madruga, D.; Sonne, M.R.; Costa, G.D.; Hattel, J.H.; Hansen, H.N. Dynamic length metrology (DLM) for accurate dimensional measurements in a production environment by continuous determination and compensation of thermal expansion effects in turning steel. *Meas. Sci. Technol.* **2021**, *32*, 094007. [CrossRef]

36. Schulte, M.J.; Omar, J.; Swartzlander, E.E. Optimal initial approximations for the Newton-Raphson division algorithm. *Computing* **2015**, *53*, 233–242. [CrossRef]

37. Bai, R.; Jiang, H.; Lei, Z.; Li, W. A novel 2nd-order shape function based digital image correlation method for large deformation measurements. *Opt. Lasers Eng.* **2017**, *90*, 48–58. [CrossRef]

38. Aborehab, A.; Kassem, M.; Nemnem, A.; Kamel, M. Miscellaneous modeling approaches and testing of a satellite honeycomb sandwich plate. *J. Appl. Comput. Mech.* **2019**, *6*, 1084–1097.